Journal of Alloys and Compounds 988 (2024) 174151

Contents lists available at ScienceDirect

Journal of Alloys and Compounds

journal homepage: www.elsevier.com/locate/jalcom

Microwave absorption properties and mechanism analyses of core-shell structured high-entropy oxides coated with PPy

Fei Zhang [a,*], Lijun Wu [a], Kai Sun [a,*], Yanhua Lei [a], Pengtao Yang [a], Hui Liu [a], Xiaosi Qi [b,*], Runhua Fan [a]

[a] College of Ocean Science and Engineering, Shanghai Maritime University, Shanghai 201306, People's Republic of China
[b] College of Physics, Guizhou University, Guiyang 550025, People's Republic of China

ARTICLE INFO

Keywords:
High-entropy oxides
Core-shell structure
Electromagnetic absorption
Magnetic losses
Impedance matching

ABSTRACT

For HEO@PPy composites, there are mainly eddy current loss and hysteresis loss in the high-entropy oxides. For the effect on the magnetic loss performance, it is weakening for Fe, Ni, and Co successively. The composite of HEO(1)-FeNi@PPy has the largest reflection loss with a minimum *RL* value of −32.04 dB and an effective absorption bandwidth of 5.8 GHz, and the corresponding thicknesses are almost the same, which enables the optimization of both parameters simultaneously. The sample also has the optimal waveband-thickness absorption characteristics. A reciprocal relationship was found between magnetic loss and dielectric loss. By incorporating the HEO(1)-FeNi@PPy powder into paraffin, it was found that the greater the amount of powder material, the higher the electric conduction loss and polarization loss, and the magnetic loss would decrease. The microwave frequency *f* was found to be the main variable affecting the magnetic permeability and dielectric constant.

1. Introduction

The advancement of modern science and technology largely relies on electronic information and the internet. As an essential medium for energy and information transmission, electromagnetic waves play a significant role in many fields, including defense, military, industrial production, and daily lives [1–3]. However, with the development of electronic communication technology, more and more electromagnetic waves are exposed in the air, generating a large amount of electromagnetic radiation. These radiations have caused various degrees of electromagnetic pollution, which not only interferes with the normal operation of certain devices and equipment but also potentially harms human health to some extent [4,5]. Therefore, how to shield or absorb excess electromagnetic waves causing pollution has become one of the hot research directions in recent years [3–5].

Microwave absorbing material is such a new type of material that allows electromagnetic waves on the material surface to enter the interior, and converts electromagnetic energy into thermal energy through various loss mechanisms, thus achieving the absorption of electromagnetic waves. Microwave absorbing materials are generally used in the form of coatings, which are more flexible and convenient to use. Through further improvements, they can achieve an absorption rate of 90% or more of the surface electromagnetic waves [6]. Moreover, with the continuous technological advancement, researchers have also developed multifunctional microwave absorbing materials with anti-corrosion, high-temperature resistance, and impact resistance, which have been applied in relevant fields [7–9]. Traditional microwave absorbing materials include ferrite [10], magnetic metal [11], and carbon materials [12]. As technology continues to advance, new microwave absorbing materials, not only possess the strong absorption of traditional microwave absorbing materials, but also meet the diversified application characteristics suitable for different fields, such as "thinner, lighter, wider, stronger". The newly developed microwave absorbing agents under investigation include nano-oxide materials, chiral materials, high-temperature-resistant ceramics, and other microwave absorbing materials [13–15]. Among them, high-entropy oxides (HEOs), as highly disordered multi-component systems, have excellent performance due to their four core effects (high-entropy effect, lattice distortion effect, sluggish diffusion effect, "cocktail" effect) [16]. They have a considerably adjustable bandgap width, maintain stability under some extreme conditions, and have the potential to prepare novel high-performance microwave absorbing materials, further

* Corresponding authors.
E-mail addresses: zhangfei@shmtu.edu.cn (F. Zhang), kais@shmtu.edu.cn (K. Sun), xsqi@gzu.edu.cn (X. Qi).

https://doi.org/10.1016/j.jallcom.2024.174151
Received 23 January 2024; Received in revised form 26 February 2024; Accepted 11 March 2024
Available online 12 March 2024

supplementing the existing microwave absorbing material system.

Since ROST and others first proposed a type of entropy-stabilized oxide ceramics in 2015 [17], high-entropy oxides have attracted much attention. After several years of research and development, high-entropy oxides with different crystal structures and constituent elements, such as rock salt type, spinel type, fluorite type, perovskite type, and so on, have been successfully prepared [18,19]. Some studies have been carried out on the absorption performance of high-entropy oxides in the microwave radio frequency band. Yan et al. [20] prepared a dual-phase high--entropy oxide $(FeCoNiZn)_xV_2O_y$ ceramic. An abundance of oxygen vacancies in the sample sintered at 900°C improved the dielectric loss performance, and the effective bandwidth was 2.77 GHz at a thickness of 2.2 mm. Zhao et al. [21] developed a high-entropy stabilized $(Ca_{0.2}Sr_{0.2}Ba_{0.2}La_{0.2}Pb_{0.2})TiO_3$ perovskite structure material, with the best effective absorption bandwidth of 1.4 GHz. Chang and others [22] synthesized high-entropy spinel ferrites $(FeCoNiCrM)_xO_y$ (M = Zn, Cu, and Mn) using solid-phase reactions. All three spinel ferrites exhibited ultra-high structural thermal stability at 800 °C. Among them, the sample containing Cu had a reflection loss value of −27.3 dB at 13.3 GHz, but the corresponding thickness was 9.1 mm. The types of absorption losses in the microwave band generally include such as magnetic loss, dielectric loss, and electrical conduction loss [23]. Although these absorbers meet the requirements of electromagnetic wave absorption efficiency, but the absorption bandwidth is not enough, need to be further improved. High-entropy oxides, as typical dielectric materials, have excellent dielectric loss performance. However, previous studies have only focused on the preparation or study of high-entropy oxides which generally has one single loss mechanism to restrict the further enhancement of wave absorption performance. It inevitably brings about certain issues such as low wave absorptivity, narrow absorption bandwidth, or thick coatings. In addition, referring to the preparation methods and results of other microwave absorbing materials with excellent performance in the literature [24–26], we would like to improve the microwave absorbing ability of high-entropy oxides even further by some methods. If the high-entropy oxides are further compounded or coated with materials with good electrical conductivity to form a core-shell structure, their electrical conduction loss and interfacial polarization loss can be improved, thereby further enhancing their wave absorption performance. Moreover, weather resistance can also be further enhanced, making them suitable not only for civilian equipment but also for military equipment such as aircraft and ships, where the working environment is more demanding. This will have real implications for future research.

In this paper, we synthesized three different high-entropy oxides by changing the types of magnetic elements contained, using a liquid-phase reaction synthesis and high-temperature sintering method. Then, we coated the outer layer with polypyrrole (PPy) to prepare core-shell structured composite materials. We studied the impact of different magnetic elements on the wave absorption performance of the high-entropy oxide core-shell structured composite materials and analyzed the intrinsic influencing mechanism in anticipation of laying a foundation for further enhancing the wave absorption performance and weather resistance of high-entropy oxides.

2. Experiment

Firstly, approximately 0.6 g metal acetate in equimolar ratios are successively added to 50 mL of water and stirred electromagnetically for 30 minutes. Then, an equal molar amount of oxalic acid relative to the acetate was weighed out to prepare a 50 mL oxalic acid solution. The prepared acetate solution was then slowly added to the oxalic acid solution, continuously stirred for another 30 minutes, and then filtered to obtain a pink precipitate. The precipitate was washed with ethanol and deionized water, and then it was sintered at 750 °C for 2 hours in a muffle furnace. Lastly, the sintered powder was ground in a ball mill to obtain the high-entropy oxide powder $(Cr_{0.2}Mn_{0.2}Cu_{0.2}Fe_{0.2}Ni_{0.2})_3O_4$ (abbreviated as HEO(1)-FeNi). According to the same method, we prepared two other high-entropy oxides, $(Cr_{0.2}Mn_{0.2}Cu_{0.2}Fe_{0.2}Co_{0.2})_3O_4$ (abbreviated as HEO(2)-FeCo) and $(Cr_{0.2}Mn_{0.2}Cu_{0.2}Co_{0.2}Ni_{0.2})_3O_4$ (abbreviated as HEO(3)-CoNi).

Secondly, 0.8 mL of pyrrole solution was mixed with deionized water and stirred for 12 minutes to prepare a 40 mL solution. Then, 0.3 g of the prepared high-entropy oxide sample was added and stirred at a speed of 550 r/min for 20 minutes to obtain a mixed solution. 40 mL of ferric chloride solution (concentration 48.75 g/L) was added to this mixture, and stirred at a speed of 650 r/min for 30 minutes. Finally, the solution was centrifuged at a speed of 5000 r/min for 20 minutes. The remaining material was dried and ground. Eventually, we successfully obtained three types of high-entropy oxide composite materials with a core-shell structure coated with polypyrrole (PPy): HEO(1)-FeNi@PPy, HEO(2)-FeCo@PPy, and HEO(3)-CoNi@PPy.

The phase structures of the prepared samples are determined by X-ray diffractometer (X'Pert PRO MPD). The morphology and microstructure of the samples are observed by scanning electron microscopy (SEM, JSM-7800 F) and transmission electron microscopy (TEM, JEM 2100 F). The room temperature magnetic hysteresis loop was measured by VSM (LakeShore, 7404). The powder sample was mixed with paraffin at a certain mass ratio, and then pressed into a ring with an outer diameter of 7 mm, an inner diameter of 3 mm, and an average HEO-mixed-paraffin thickness of 3 mm using a mold. The electromagnetic parameters of the sample in the frequency range of 2–18 GHz are tested by a vector network analyzer (Keysight N5244A, USA).

3. Results and discussion

3.1. Structure and morphology

To verify the synthesis of high-entropy oxides and the encapsulation effect of PPy on the oxides, SEM tests are conducted on HEO(1)-FeNi and HEO(1)-FeNi@PPy, with the results shown in Fig. 2. From Fig. 2(a)-(c), it can be seen that the particle size of the prepared high-entropy oxide particles is around 1 μm. The uncoated HEO in Fig. 2(a) tends to agglomerate, making the particle size shape not clear. But after coating, the particle size shape of the HEO (Fig. 2(b)–(c)) is more obvious, indicating that the HEO powder coated with PPy can effectively reduce the agglomeration effect of particle size. Fig. 2(a) also shows that each powder particle contains many grains with a diameter of about 50 nm, and the grains show a typical spinel structure (as shown in the enlarged image in the box in Fig. 2(a)). Analysis of XRD diffraction also revealed that the HEO(1)-FeNi powder exhibits a typical spinel structure (as shown in Fig. 3(a)). Taking the half-peak width of the (311) crystal plane as an example, the grain size obtained by applying the Scherrer formula is about 40 nm, which is basically consistent with the SEM observation results. Fig. 2(c) shows that the thickness of the coated PPy is about 200–300 nm. In Fig. 2(a) and (b), the thickness of PPy leads to an increase in the particle size of the coating by about 500 nm. Fig. 2(d) shows that PPy is successfully coated on the surface of the high-entropy oxide, and the interface between PPy and HEO powder is well combined. The high-entropy oxide on the right has clear lattice stripes, indicating that the HEO has a good crystal structure. The magnified image shows that the selected grain exhibits a clear (440) crystal plane, with a interplanar spacing of 1.24 Å. Fig. 2(e) is the TEM diffraction spectrum of the HEO(1)-FeNi sample. It can be seen that only the (220), (311), and (440) crystal planes exhibit obvious diffraction rings, corresponding to the three diffraction peaks with the highest intensity in the XRD diffraction spectrum. The (311) peak in XRD has the largest intensity, and the diffraction ring of the (311) crystal plane in TEM is also the most obvious (Fig. 2(d)). Since the grain size in the prepared powder is larger, some bright spots also appear in the TEM diffraction ring scattered on the ring. We analyze the distribution of metal elements in the area of Fig. 2(f), just as the mapping in Fig. 2(g)-(k). It is found that the content of five metal elements in the high-entropy oxide are evenly distributed,

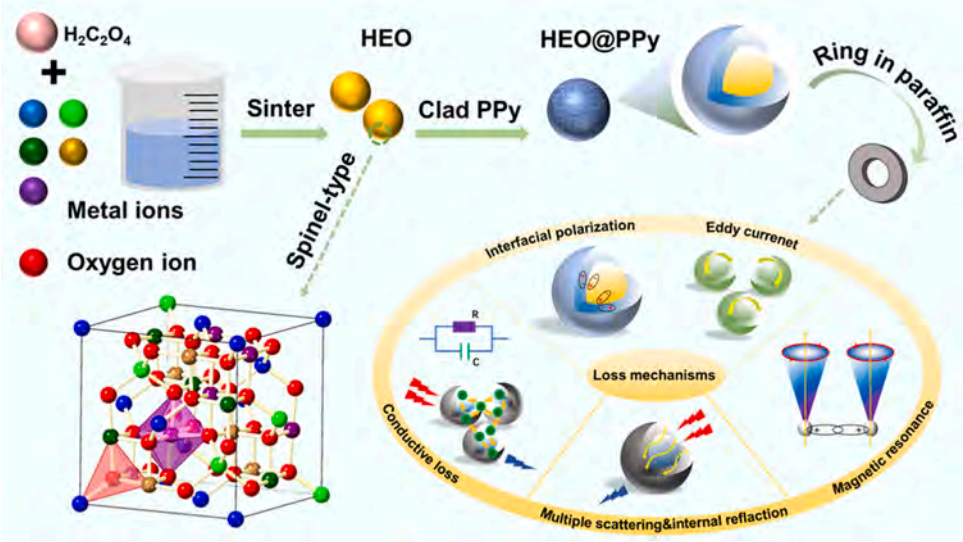

Fig. 1. Preparation and electromagnetic wave absorption mechanism of core-shell structured HEO@PPy composite materials.

indicating the successful synthesis of high-entropy oxides. Fig. 2(l) is the distribution of N elements contained in the coated PPy, which illustrates the uniform and the excellent coating effect.

3.2. Physical characteristics

Fig. 3(a) shows the XRD patterns of different high-entropy oxides. By comparing with PDF cards, it is found that the crystal structure of the synthesized high-entropy oxide powder is a typical spinel structure. At the same time, however, there are many distinct companion peaks near the (311), (222), and (400) crystal planes in the spectra, which are mainly due to lattice distortions caused by high-entropy materials containing multiple elements. Lattice distortion is one of the four central effects of high-entropy oxides [18], where different atomic sizes lead to deformation of the crystal structure. As shown in the upper left corner, when the doped ion diameter is not too large, it can cause a slow change in the lattice constant and crystal plane spacing (as shown by the two red arrows above the ions in the upper left inset). This gentle change can cause the main diffraction peaks to shift left or right (the (311) peak for HEO(3)-CoNi shifts left, while the (311) peak for HEO(1)-FeNi shifts right). It should be noted that a large diameter of the doped ion can cause an abrupt change in the lattice constant and crystal plane spacing (such as the ion shown by the single red arrow below in the top left inset). This mutation may result in the appearance of companion peaks next to the main XRD diffraction peaks.

From Fig. 3(b), HEO(1)-FeNi has a higher saturation magnetization intensity, followed by HEO(2)-FeCo@PPy, HEO(3)-CoNi@PPy. It can be seen that the following relationship exists for the enhancement of magnetization intensity: Fe>Ni>Co. According to the literature [27], in high-entropy oxides, Fe ions generally contain Fe^{2+} and Fe^{3+} cations, Ni ions are generally Ni^{2+}, and Co ions are generally Co^{2+} or Co^{3+}. For 3d transition group metal oxides, the outer electrons determine the magnetic properties, but their positions are susceptible to the crystal fields of the surrounding elements in the solid, which results in the solidification of the orbital angular momentum of the electrons [28–30]. Thus, the ionic magnetic moment in metal oxides is mainly determined by the electronic spin magnetic moment. And based on the electron arrangement of the 3d transition metal, the total magnetic moment of the electronic spin moment of the outermost trivalent and divalent ions is 5 μ_B and 4 μ_B, respectively (μ_B is the Bohr magneton) [31]. The saturation magnetization intensity of HEO(1)-FeNi is greater than that of HEO (2)-FeCo, and the difference between the two is only the Ni and Co elements. Since the Ni ion is Ni^{2+}, it means that HEO(2)-FeCo also contains only Co^{2+} element. Moreover, the orbital magnetic moments of Ni^{2+} cation is larger than those of Co^{2+} cation, indicating that they are less affected by the external crystal field and have relatively large orbital magnetic moments.

After coating PPy, there are two effects: firstly, the content of high entropy oxides is reduced at the same mass fraction, which leads to a decrease in its saturation magnetization strength. The other is that after coating PPy with better conductivity, partial proximity or linkage between the powders occurs. Under the action of alternating currents produced by the incident microwave, they can be regarded as capacitors and inductors respectively, forming a similar LC oscillation circuit (as shown in the Conductive Loss in Fig. 1) [32]. Thereby, under an alternating electric field, a conduction-like current path can be generated within the PPy coatings even if they are not in contact [33–35]. Moreover, the induced micro-currents generated by the outside-coated PPy can also affect the crystal fields of the coated metal ions to reduce the electron exchange of the magnetic ions, and thus decreasing the saturation magnetization strength of this material. As a result, we found that the saturation magnetization strength of all the samples with coated PPy was drastically reduced (as shown in Fig. 3(b)). As can be seen from the figure, the coercivity of the HEO(1)-FeNi@PPy sample increases from 100 Gs to 300 Gs after coating. It indicates that the induced micro-current within the PPy coating on the outside of the HEO(1)-FeNi produces a magnetic field that hinders the change of this micro-current (i.e. hindering the change of this magnetic field), which is far greater than the weakening effect of the ability to resist magnetic field change due to the reduction in oxide content. Moreover, this hindering effect further reduces the saturation magnetization intensity, resulting in a lower saturation magnetization intensity for the HEO(1)-FeNi@PPy sample than that of HEO(2)-FeCo@PPy sample. However, the HEO (2)-FeCo@PPy sample has a lower coercivity from 100 Gs to 50 Gs in contrary, indicating that the impact of the lower high-entropy oxide content on the change of magnetic field outweighs the hinder effect on this change. This phenomenon also reflects that the HEO(2)-FeCo sample has a lower magnetization ability compared with the HEO(1)-FeNi sample, and this speculation is confirmed by the fact that the saturation magnetization intensity of the HEO(2)-FeCo sample is indeed smaller than that of the HEO(1)-FeNi sample just as shown in Fig. 3(b). These results above suggest that the coated HEO(1)-FeNi@PPy sample can produce the highest hysteresis loss, followed by the coated HEO (2)-FeCo@PPy and HEO(3)-CoNi@PPy samples. In other words, there exist both the eddy current loss caused by the micro-current inside PPy and the hysteresis loss caused by the high-entropy oxide. And the

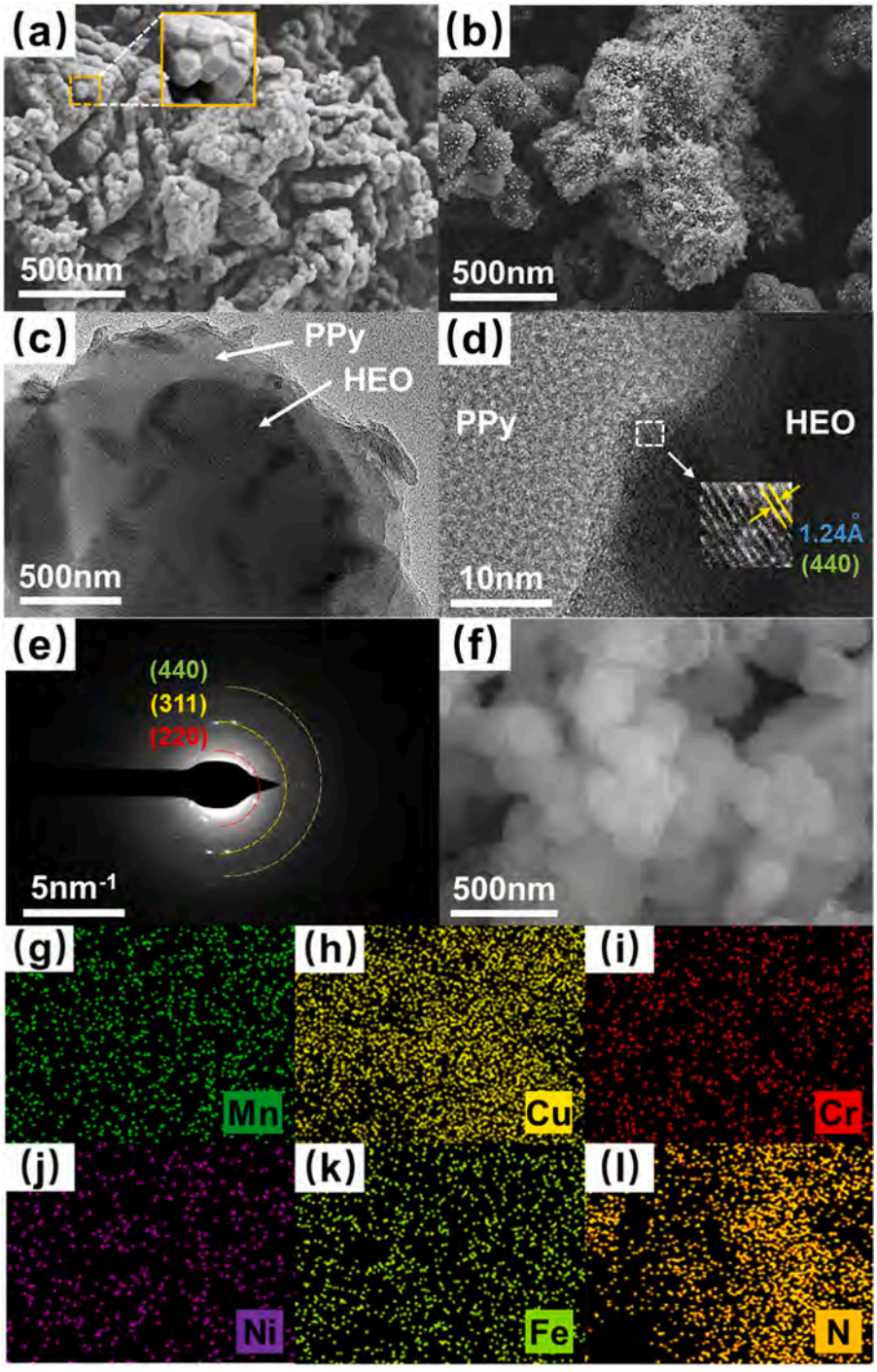

Fig. 2. SEM images: (a) HEO(1)-FeNi; (b) HEO(1)-FeNi@PPy. For HEO(1)-FeNi@PPy, (c)-(e): TEM images. (f)-(l): Mapping images.

elements that affect the strength of this comprehensive magnetic loss in order are Fe, Ni, Co.

3.3. Microwave absorption property analysis

The electromagnetic parameters of the material are tested in the frequency band 2–18 GHz using vector network analyser. The *RL* values are calculated according to the formula (2) and the graphs are plotted as below.

The above three Fig. 4(a)-(c) are curves drawn by calculating the reflection loss (*RL*) values at different HEO-mixed-paraffin thicknesses for the three high-entropy oxides mixed at the mass ratio 20 wt% in paraffin. The horizontal axis is the frequency, and the vertical axis is the *RL* value. Based on the transmission line theory, the key index *RL* for evaluating the absorption characteristics of electromagnetic waves can be derived from the following formulas [36].

$$Z = \left|\frac{Z_{in}}{Z_0}\right| = \sqrt{|\mu_r/\varepsilon_r|}\tanh\left[j\left(\frac{2\pi fd}{c}\right)\sqrt{\mu_r\varepsilon_r}\right] \quad (1)$$

$$RL = 20\log|(Z_{in} - Z_0)/(Z_{in} + Z_0)| \quad (2)$$

where Z_{in} is the normalized input impedance of the absorbing material, Z_0 is the free space impedance, ε_r is the complex permittivity, μ_r is the complex permeability, f is the frequency, c is the speed of light in free

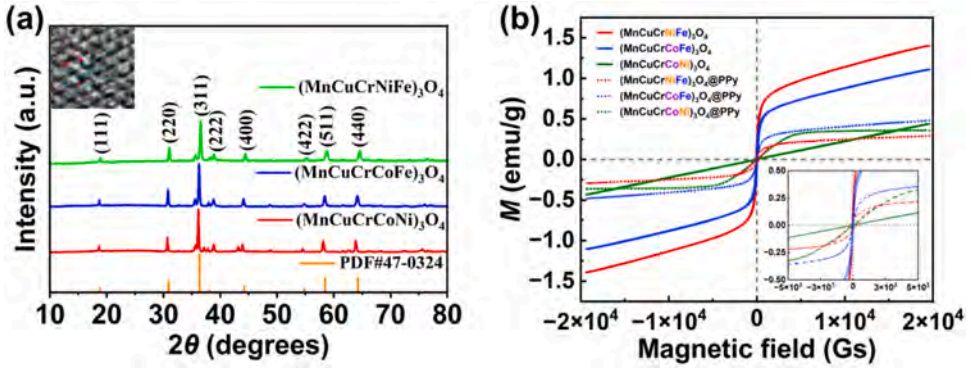

Fig. 3. (a) XRD spectra of different HEO@PPy (note: the upper left corner shows the lattice distortion caused by the doping ions); (b) Hysteresis curves at room temperature.

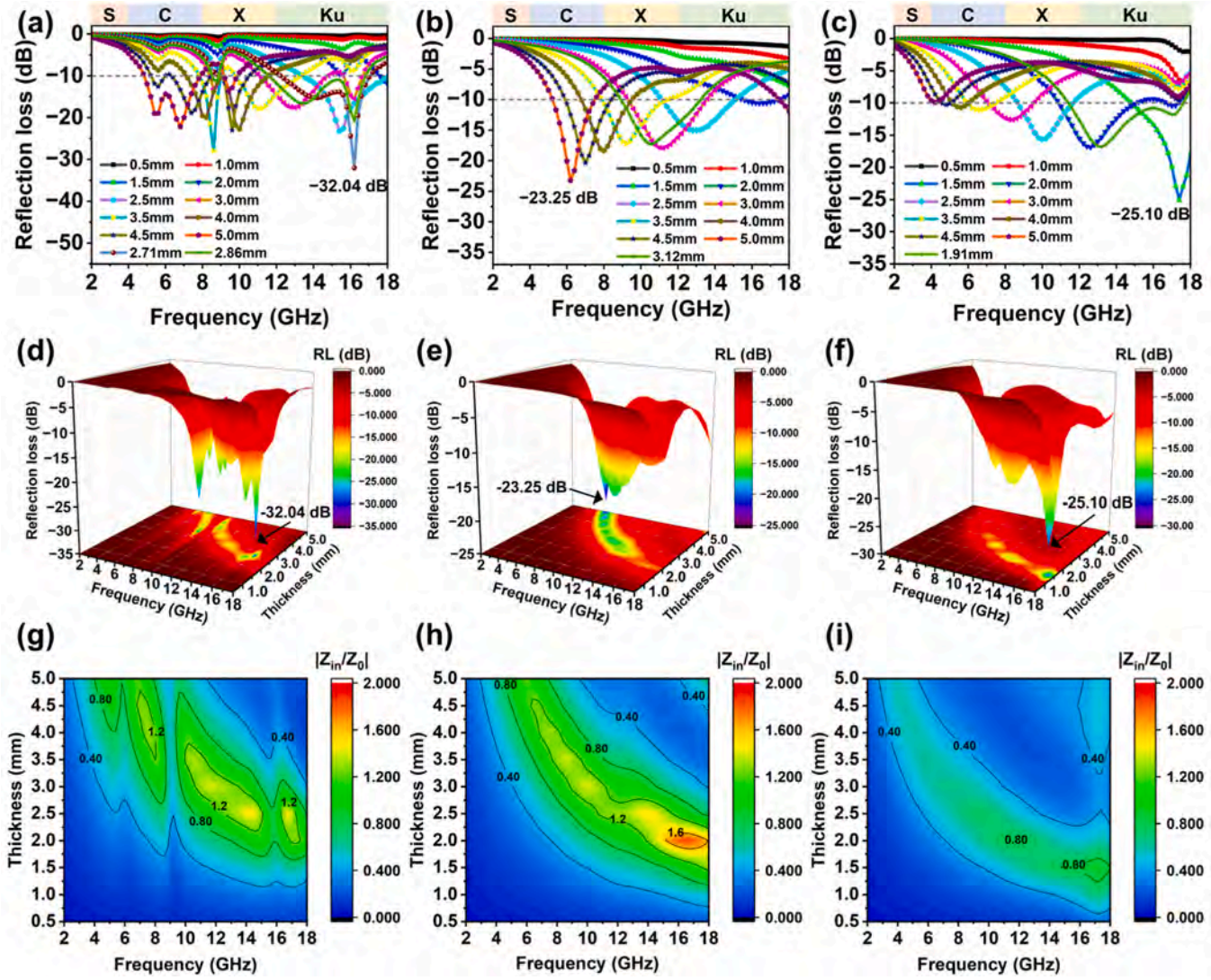

Fig. 4. Two-dimensional *RL* curves: (a) HEO(1)-FeNi@PPy; (b) HEO(2)-FeCo@PPy; (c) HEO(3)-CoNi@PPy. Three-dimensional *RL* curves: (d) HEO(1)-FeNi@PPy; (e) HEO(2)-FeCo@PPy; (f) HEO(3)-CoNi@PPy. Impedance matching $|Z_{in}/Z_0|$ contour plots: (g) HEO(1)-FeNi@PPy; (h) HEO(2)-FeCo@PPy; (i) HEO(3)-CoNi@PPy.

space, and *d* is the thickness of the absorber (HEO-mixed-paraffin). By calculating *RL*, the efficiency of the sample in absorbing the electromagnetic wave can be judged.

According to the literature [37], when the *RL* value is below −10 dB, the electromagnetic wave absorption rate of the material can reach to 90%, which is effective absorption. The maximum bandwidth with *RL* value continuously less than −10 dB is the maximum effective absorption bandwidth. In order to better evaluate the microwave absorbing properties of the materials, we divide the 2–18 GHz band into four parts, which are S (2–4 GHz), C (4–8 GHz), X (8–12 GHz) and Ku (12–18 GHz).

According to the grey dashed reference line in Fig. 4, we can see that the composites perform better overall in the range of 0–5.0 mm for HEO-mixed-paraffin thicknesses, with *RL* value peaks all below −10 dB. Among them, the composite with 20 wt% HEO(1)-FeNi@PPy has the highest reflection loss, with the best *RL* value of −32.04 dB at the HEO-mixed-paraffin thickness of 2.71 mm, with the main absorption frequency band of the material in the Ku band at this time. Furthermore, the effective absorption bandwidth ($RL \leq -10$ dB) of the composite is maximum (5.8 GHz) at a thickness of 2.86 mm. In contrast, the component of HEO(2)-FeCo@PPy has a too big theoretical thickness of 5 mm corresponding to the minimum reflection loss with a *RL* value −23.25 dB. Even the minimum reflection loss of HEO(3)-CoNi@PPy is only −25.10 dB, which is all less than −32.04 dB. By comparison, we find that HEO(1)-FeNi@PPy has the widest effective absorption band, spanning the three bands C-Ku. And there are multiple peaks in this band range, indicating excellent microwave absorption performance.

Fig. 4(d)-(f) show the three-dimensional projection diagrams of the reflection loss. From the figures, it can be seen that the greater thickness corresponds to the lower the frequency of the effective absorption band. The projection of the *RL* peak gradually moves to the direction of lower frequency as the thickness increases. This phenomenon can be explained by the quarter-wavelength theory with the following formula [38]:

$$d = \frac{n\lambda}{4} = \frac{nc}{4f\sqrt{|\varepsilon_r||\mu_r|}} \quad (n = 1, 3, 5\cdots) \tag{3}$$

where λ denotes the wavelength. From the formula, we can see that when other parameters keep unchanged, the thickness d is inversely proportional to the frequency f. Thus, when the thickness d continuously increases, the frequency f will gradually decrease. The theoretical derivation is consistent with the experimental results. It also can be seen that the HEO(1)-FeNi@PPy mixed-paraffin sample has uniform *RL* values within the test frequency range. As the test frequency increases and the thickness decreases, the *RL* value of the HEO(2)-FeCo@PPy mixed-paraffin sample gradually decreases, while the HEO(3)-CoNi@PPy sample gradually increases. The thickness corresponding to the maximum *RL* value and the widest *RL* value of HEO(1)-FeNi@PPy sample is almost the same, so it is possible to optimize these two parameters simultaneously, which is very important for practical applications. For the HEO(3)-CoNi@PPy mixed-paraffin sample, the full profile of the width of the maximum *RL* value could not be displayed as it exceeded the measurement range. However, the trend of the curves illustrates that the width is still large and has important application prospects at higher frequencies.

It can be seen from Fig. 4 and Table 1 that for a given HEO-mixed-paraffin thickness, the frequency of the electromagnetic wave corresponding to the peak reflectivity of the sample shifts to the left in sequence [39], such as the frequency corresponding to the peak reflectivity of the 2.5 mm thickness with the redshifts of the sequence 15.3 GHz, 13 GHz, and 10 GHz. This leads to the HEO-mixed-paraffin thickness decreasing in sequence at a certain frequency for the absorption of electromagnetic waves (for example, at 16 GHz, the thicknesses of the three samples correspond to 2.5 mm, 2 mm, 1.5 mm in sequence). By comparison, it can be found that HEO(3)-CoNi@PPy mixed-paraffin requires the smallest thickness, which will reduces the weight of its coating in practical applications, and this is of great practical importance. Since the three HEOs are coated with the same amount of PPy, there is not much difference in the conductive loss, and the main reasons for this difference are polarization loss and magnetic loss. According to the previous hysteresis loop analysis, the HEO(3)-CoNi@PPy sample has the worst magnetization ability. The $\tan\delta_\mu$ plot in Fig. 5(f) shows that its magnetic loss factor is the lowest, but its dielectric loss ability is the strongest (as shown in the $\tan\delta_\varepsilon$ in Fig. 5(c)). Fig. 5 also illustrates the inverse relationship between magnetic and dielectric losses in an alternating electromagnetic field. This is mainly due to the fact that the HEO coated with conductive polymer PPy can produce a magnetization that hinders the change of the alternating electric field, and can also produce a polarization that complies with the change of the alternating electric field. The two effects are contradictory to each other [40]. Fig. 3 illustrates that the magnetization ability of HEO(3)-CoNi@PPy mixed-paraffin is the weakest, which leads to the lowest magnetic loss, but its dielectric loss is the highest. Generally, the attenuation coefficient α is also an important factor that influences the reflection loss and determines the attenuation characteristics of the material. According to the transmission line theory and electromagnetic wave propagation constant, the derivation formula of the attenuation coefficient α is as follows [41]:

$$\alpha = \frac{\sqrt{2}\pi f}{c}\sqrt{\left(\mu_r''\varepsilon_r'' - \mu_r'\varepsilon_r'\right) + \sqrt{\left(\mu_r''\varepsilon_r'' - \mu_r'\varepsilon_r'\right)^2 + \left(\mu_r''\varepsilon_r'' + \mu_r'\varepsilon_r'\right)^2}} \tag{4}$$

Notably, the larger the attenuation coefficient α, the stronger the ability to attenuate electromagnetic waves. Fig. 5(h) illustrates that the attenuation coefficient α of HEO(3)-CoNi@PPy mixed-paraffin is also greater than those of HEO(1)-FeNi@PPy and HEO(2)-FeCo@PPy samples. Therefore, HEO(3)-CoNi@PPy sample has the optimum monochromatic wave absorption ability and the thinnest absorption thickness for wave absorption at the same frequency.

Additionally, we also need to research the width of the absorption waveband of the samples. As can be seen from Fig. 4(a)–(c), the nearest reflection loss peaks near 18 GHz for the three samples correspond to thicknesses of 2.5 mm, 2.0 mm, and 1.5 mm, respectively, but the left side exhibits strong absorption (<-10 dB) in the vicinity of 5 GHz for all samples. This brings about a decrease in the ratio of the effective absorption bandwidth to thickness (Effective bandwidth/thickness). That is to say, the average absorption width per unit of thickness decreases in the order of 5.3 GHz/mm, 4.2 GHz/mm, and ~3.8 GHz/mm (Table 1), respectively. This means that the HEO(1)-FeNi@PPy mixed-paraffin sample has the best band-absorption characteristics (waveband-thickness absorption characteristics) on the whole, while HEO(3)-CoNi@PPy sample has the lowest band-absorption characteristics comparably. For

Table 1
Data of parameters related to reflection loss.

	Maximum reflection loss			Widest reflection loss			Rat. (GHz/mm)		Wf. (GHz)
	Pv. (dB)	Ct. (mm)	Eab. GHz)	Fr. (dB)	Ct. (mm)	Pcf. (GHz)			
HEO(1)-FeNi@PPy	-32.04	2.71	4.9	5.8	2.86	21	5.3	15.3	
HEO(2)-FeCo@PPy	-23.25	5	2.3	4.3	3.12	17.5	4.2	13	
HEO(3)-CoNi@PPy	-25.10	1.5	~4	6.3	1.91	17	~3.8	10	

Pv.: Peak value; **Ct.**: Corresponding thickness; **Eab.**: Effective absorption bandwidth;
Fr.: Frequency range; **Pcf.**: Peak corresponding frequency;
Rat.: Ratio of effective absorption bandwidth to thickness (Effective bandwidth/thickness);
Wf.:Wave frequency corresponding to peak reflectivity of 2.5 mm thickness.

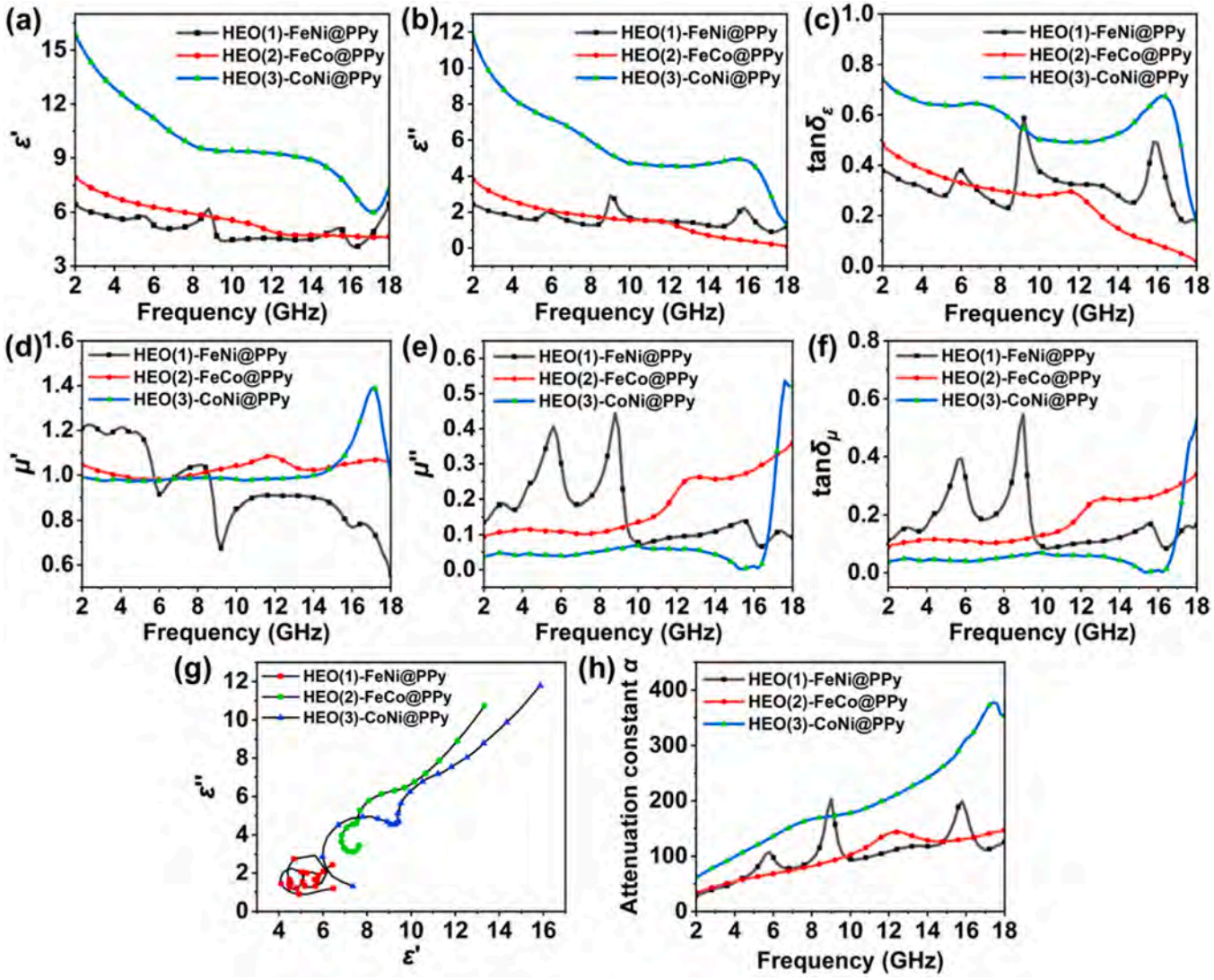

Fig. 5. (a) Real part of permittivityε'; (b) Imaginary part of permittivityε''; (c) Dielectric loss tangent $\tan_{\delta\varepsilon}$;(d) Real part of permeability μ'; (e) Imaginary part of permeability μ''; (f) Magnetic loss tangent $\tan_{\delta\mu}$; (g) Cole-Cole plots ε'-ε''; (h) Attenuation constant α.

the widest reflection loss value, as a an important index, it can be seen from Table 1 that the broadest value of the HEO(3)-CoNi@PPy sample is 6.3 GHz at a thickness of 1.91 mm, while the broadest value of the HEO (1)-FeNi@PPy sample is 5.8 GHz at a thickness of 2.81 mm. Furthermore, both of them cover a similar wide band range of about 11.5–17 GHz. Therefore, the difference is not significant, but HEO(3)-CoNi@PPy mixed-paraffin has a smaller thickness. From this perspective, HEO(3)-CoNi@PPy sample performs better than HEO(1)-FeNi@PPy sample. However, since HEO(3)-CoNi@PPy sample has the lowest band-absorption characteristics (~3.8 GHz/mm), it is inevitable to subject to large absorption band offset due to thickness errors in practice, which reduces its operability. In contrast, the HEO(1)-FeNi@PPy sample has stronger operability (optimal band-absorption characteristic 5.3 GHz/mm).

Impedance matching is also a fundamental physical quantity to the microwave absorption performance of materials, which reflects the ability of electromagnetic waves to enter and be lost inside the microwave absorbing materials [42,43]. According to formula (1) [44], when Z=1, the reflection coefficient is 0, indicating that the electromagnetic wave incident perpendicular from the free space to the interface of the microwave absorbing material can achieve zero reflection, which is complete impedance matching at this time. When Z=0, the reflectivity is 1, indicating that the electromagnetic wave undergoes the phenomenon of total reflection. Whereas, formula (2) explains that the impedance matching is related to the electromagnetic parameters and thickness of the absorber. Therefore, to be more intuitive, we plotted the impedance matching contour plots just as shown in Fig. 4(g)–(i). It can be confirmed that the part of Z=1 corresponds to the green area in the figure. The larger the area corresponding to the green color, the better the impedance matching of the sample. For better quantitative evaluation, we categorized all values in the range of 0.8–1.2 as good impedance matching performance. Obviously, the figure shows that HEO (1)-FeNi@PPy mixed-paraffin and HEO(2)-FeCo@PPy mixed-paraffin have better impedance matching.

We further analyze the absorption mechanism by means of the Cole-Cole plot (Fig. 5(g)). The abscissa of the Cole-Cole plot of HEO@PPy mixed-paraffin is the real part of the complex dielectric constant, and the ordinate is the imaginary part of the complex dielectric constant. The appearance of a semicircle in the curve in the Cole-Cole plot indicates the presence of a Debye relaxation process [45]. The more Debye semicircles, it means that the polarization ability and dielectric loss of the material is stronger [46]. Fig. 5(g) indicates that a certain amount of Debye semicircle exists in all three HEO-mixed-paraffin samples, which means that polarization relaxation exists in all three samples during wave absorption. This is mainly due to the fact that high-entropy oxide particles coated with amorphous PPy will inevitably produce certain

defects at the interface. When the microwave passes through these defects, it will form a polarization center and form a Debye semicircle [47]. By comparison, it is found that although the HEO(1)-FeNi@PPy sample curves have the most Debye semicircles, none of the polarization intensities are too strong and there is no significant conductivity loss, suggesting that they are mainly magnetic losses. However, the polarization losses of HEO(2)-FeCo@PPy and HEO(3)-CoNi@PPy samples are obviously increasing in sequence, and they both have a certain conductive loss, which is consistent with the previous analysis results.

The comparison of Fig. 5(c) and (f) shows that the polarization loss and magnetic loss in the same sample present an obvious inverse relationship, which proves that the inverse relationship between polarization loss and magnetic loss is also applicable within the same sample. For the same composite sample, the micro-current generated by the PPy therein is small at low frequencies, and the magnetic loss of the coated high-entropy oxide is low too, while the polarization loss is relatively large. It can be seen from Fig. 5(e) that the HEO(3)-CoNi@PPy mixed-paraffin does have a strong polarization resonance than the HEO(2)-FeCo@PPy sample. Meanwhile, HEO(1)-FeNi@PPy sample has a strong magnetization ability, and so the reduced micro-current can still produce strong magnetization, and even two magnetic resonance peaks exist in the low frequency band [48]. Therefore, it can still produce strong magnetic loss in the low frequency band. With the increase of electromagnetic wave frequency, the micro-current generated by PPy in the same sample becomes larger, leading to a gradual increase in the magnetic loss of the coated high-entropy oxides, while its polarization loss gradually decreases, which is more obvious for the HEO (3)-CoNi@PPy and HEO(2)-FeCo@PPy samples (shown in Fig. 5(c)).

From the above analysis, we find that for different components of HEOs@PPy, after mixing with paraffin (HEO-mixing) at a mass ratio of 20 wt%, the overall absorption effect of HEO(1)-FeNi@PPy sample is the best. In order to further study the effect of HEO-mixing mass ratio on the absorption performance, we changed the HEO-mixing mass ratio to be 20 wt%, 35 wt%, 50 wt%, and further tested the related parameters. The results and analyses are as follows.

By comparing the *RL* graphs, it indicates that the wave absorption properties of the composites gradually decrease as the HEO-mixing mass ratio increases. The *RL* values in the range of 2–18 GHz are basically above −10 dB, indicating that the electromagnetic wave absorption is generally below 90%. It means that the electromagnetic wave reflection is enhanced with the increase of HEO-mixing mass ratio. According to the comparison of Fig. 6(c) and (f), the impedance matching performance of the material gradually decreases. Although the attenuation coefficient α increases with increasing content (Fig. 6(m)), the large amount of reflected electromagnetic waves from the material prevents them from entering the material, resulting in a gradual deterioration of its microwave absorbing performance. According to formula (1), the mismatch between the composite permeability and dielectric constant caused by the increase in HEO-mixing mass ratio can make the impedance matching deviate from the optimal value “1”. In addition, according to the dielectric loss factor $\tan\delta_\varepsilon$ (Fig. 6(i)), the dielectric loss gradually increases with the increase of HEO-mixing mass ratio, while its magnetic loss gradually decreases (Fig. 6(l)). Furthermore, this also causes the absolute valueof the ratio of complex permittivity ε_r and complex permeability $|\mu_r/\varepsilon_r|$ to decrease, giving rise to a decrease in the value of $|Z_{in}/Z_0|$, and this trend can also be shown in Fig. 6(d)-(f). (Note: the legends of (e) and (f) here are different from (d) to make the pictures more aesthetically pleasing, but they do not affect the results of the analysis).

In addition, several peaks appear in the complex dielectric constant curve of the 20 wt% sample, which are not observed in the samples of other proportions. These peaks correspond to the phenomenon of polarization relaxation. Combined with the previous analysis, the dielectric loss of the material at this ratio is weak. But after increasing the mass ratio, the conductivity of the sample is also enhanced, and the loss mechanism changes to be dominated by dielectric and conductive losses, which suppresses the generation of polarization relaxation peaks.

Fig. 6(j)–(l) shows the relevant parameters of complex magnetic permeability. It can be seen that as the frequency increases, the 20 wt% curve exhibits three distinct magnetic resonance peaks near 5 GHz, 9 GHz and 16 GHz, while the other three curves have no such peaks. This creates more pathways for PPy contact conduction, which increases the conductivity loss and polarization loss. This naturally reduces the magnetic resonance and eddy current effects formed inside the material [49], thus reducing magnetic loss.

Fig. 6(n) reveals that as the mass ratio of HEO(1)-FeNi@PPy powder in the mixed-paraffin composite increases, the lowest reflection peak $|RL_{min}|$ corresponding to the same thickness shifts to the left sequentially. Taking 2.5 mm thickness as an example, the absorption peak $|RL_{min}|$ shifts to the left (towards the low frequency direction) with the increasing mixed-paraffin mass ratio. This is mainly due to the fact that, the change of magnetic permeability and dielectric constant with the HEO@PPy content is smaller than the change with the microwave frequency *f*, which results in the microwave frequency *f* being the main variable in the *RL* formula (1), leading to significant changes of the *Z* value. This also leads to an enhancement of the impedance matching value $|Z_{in}/Z_0|$ along with increasing microwave frequency *f* in the same sample (as shown in Fig. 6(d)–(f)).

4. Conclusions

We have investigated three different components of core-shell structured HEO@PPy composites and analyzed the electromagnetic microwave absorbing properties and related mechanisms. It is found that there are eddy current loss caused by micro-current in PPy and hysteresis loss generated in high-entropy oxides, and the elements that affect the strength of magnetic loss are Fe, Ni and Co in order. Among these samples, HEO(1)-FeNi@PPy mixed-paraffin has the largest reflection loss, with a *RL* value −32.04 dB at the thickness of 2.71 mm and an effective absorption bandwidth (*RL*<-10 dB) of 5.8 GHz. Furthermore, the thickness corresponding to the maximum and widest reflection loss values are almost the same, and the optimization of these two parameters can be achieved at the same time. Moreover, the HEO (1)-FeNi@PPy sample has the optimal band-absorption characteristic (5.3 GHz/mm), and the absorption band offset due to the thickness deviation is small in practical application, which is highly operable for practical application. The HEO@PPy is found to exhibit a reciprocal relationship between the magnetic and dielectric losses. By comparing different mass ratios of HEO(1)-FeNi@PPy mixed-paraffin samples (20 wt%, 35 wt%, 50 wt%), the increasing content brings about the formation of contact conduction of PPy, which leads to the increasing conductivity loss and polarization loss, and reduce the magnetic loss. It is also found that for the same sample, the change of magnetic permeability and dielectric constant with the HEO@PPy content is smaller than the change with the microwave frequency *f*, making the microwave frequency *f* being the main variable, and consequently the impedance matching value $|Z_{in}/Z_0|$ in the same sample is enhanced with the increasing *f* value.

In conclusion, the high-entropy oxides have great advantages of preparing new microwave absorbing materials with the properties “thinner, lighter, wider, stronger”. The conclusions of this paper will lay a certain theoretical foundation for further study in this field, and it has important reference value for practical application.

CRediT authorship contribution statement

Fei Zhang: Writing – review & editing, Writing – original draft, Formal analysis, Data curation, Conceptualization. **Lijun Wu:** Investigation, Writing-Original Draft. **Kai Sun:** Conceptualization, Methodology, Writing-Review & Editing. **Yanhua Lei:** Formal analysis. **Pengtao Yang:** Testing, Investigation. **Hui Liu:** Investigation. **Xiaosi Qi:** Supervision. **Runhua Fan:** Supervision, Funding acquisition.

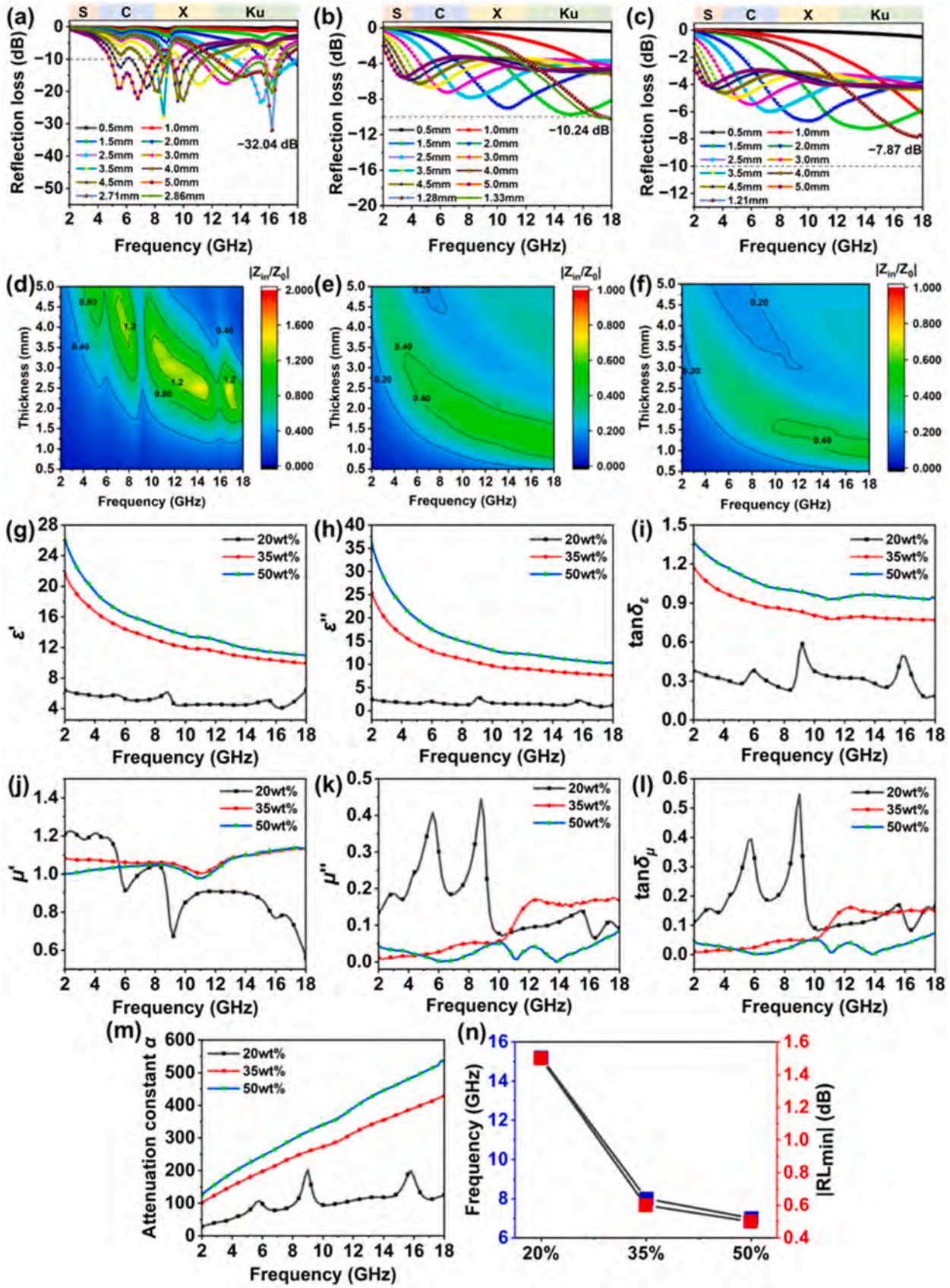

Fig. 6. For HEO(1)-FeNi@PPy mixed-paraffin composites: *RL* curves of (a) 20 wt%; (b) 35 wt%; (c) 50 wt%. Contour maps of $|Z_{in}/Z_0|$ (d) 20 wt%; (e) 35 wt%; (f) 50 wt%. (g) Real part of permittivity ε'; (h) Imaginary part of permittivity ε''; (i) Dielectric loss tangent $\tan\delta_\varepsilon$; (j) Real part of permeability μ'; (k) Imaginary part of permeability μ''; (l) Magnetic loss tangent $\tan\delta_\mu$; (m) Attenuation constant α; (n) Plots of *f* and *RL* versus mass ratios at 2.5 mm thickness.

Declaration of Competing Interest

The authors declare that they have no known competing financial interests or personal relationships that could have appeared to influence the work reported in this paper.

Data Availability

Data will be made available on request.

Acknowledgements

This work was financially supported by the Science and Technology Commission of Shanghai Municipality (20ZR1423400, 22ZR1426800); National Natural Science Foundation of China (52271182, 52071329); Shanghai Engineering Technology Research Centre of Deep Offshore Material (19DZ2253100).

References

[1] F. Qin, C. Brosseau, A review and analysis of microwave absorption in polymer composites filled with carbonaceous particles, J. Appl. Phys. 111 (2012) 061301.
[2] Z. Gao, B. Xu, M. Ma, A. Feng, Y. Zhang, X. Liu, Z. Jia, G. Wu, Electrostatic self-assembly synthesis of $ZnFe_2O_4$ quantum dots ($ZnFe_2O_4$@C) and electromagnetic microwave absorption, Compos. Part B: Eng. 179 (2019) 107417.
[3] H. Wang, F. Meng, F. Huang, C. Jing, Y. Li, W. Wei, Z. Zhou, Interface modulating CNTs@PANi hybrids by controlled unzipping of the walls of CNTs to achieve tunable high-performance microwave absorption, ACS Appl. Mater. Interfaces 11 (2019) 12142–12153.
[4] Y. Xia, W. Gao, C. Gao, A review on graphene-based electromagnetic functional materials: electromagnetic wave shielding and absorption, Adv. Funct. Mater. 32 (2022) 2204591.
[5] H. Xu, X. Yin, M. Li, F. Ye, M. Han, Z. Hou, X. Li, L. Zhang, L. Cheng, Mesoporous carbon hollow microspheres with red blood cell like morphology for efficient microwave absorption at elevated temperature, Carbon 132 (2018) 343–351.
[6] Y. Wang, S. Yang, H. Wang, G. Wang, X. Sun, P. Yin, Hollow porous CoNi/C composite nanomaterials derived from MOFs for efficient and lightweight electromagnetic wave absorber, Carbon 167 (2020) 485–494.
[7] L. Song, F. Zhang, Y. Chen, L. Guan, Y. Zhu, M. Chen, H. Wang, B.R. Putra, R. Zhang, B. Fan, Multifunctional SiC@SiO_2 nanofiber aerogel with ultrabroadband electromagnetic wave absorption, Nano-Micro Lett. 14 (2022) 152.
[8] T. Chen, Y. Tian, Z. Guo, Y. Chen, Q. Qi, F. Meng, Design of novel RGO/2D strip-like ZIF-8/DMAOP ternary hybrid structure towards high-efficiency microwave absorption, active and passive anti-corrosion, and synergistic antibacterial performance, Nano Res. 11 (2023) 5974.
[9] Y. Lin, X. Yang, Y. Huang, M. Chen, Impact-resistant multilayered metastructure for broadband microwave absorption designed by evolutionary optimization, Compos. Struct. 272 (2021) 114235.
[10] J. Ding, L. Wang, Y. Zhao, L. Xing, X. Yu, G. Chen, J. Zhang, R. Che, Boosted interfacial polarization from multishell TiO_2@Fe_3O_4@PPy heterojunction for enhanced microwave absorption, Small 15 (2019) e1902885.
[11] J. Xiang, J. Li, X. Zhang, Q. Ye, J. Xu, X. Shen, Magnetic carbon nanofibers containing uniformly dispersed Fe/Co/Ni nanoparticles as stable and high-performance electromagnetic wave absorbers, J. Mater. Chem. A 2 (2014) 16905–16914.
[12] C. Wang, V. Murugadoss, J. Kong, Z. He, X. Mai, Q. Shao, Y. Chen, L. Guo, C. Liu, S. Angaiah, Z. Guo, Overview of carbon nanostructures and nanocomposites for electromagnetic wave shielding, Carbon 140 (2018) 696–733.
[13] C. Oses, C. Toher, S. Curtarolo, High-entropy ceramics, Nat. Rev. Mater. 5 (2020) 295–309.
[14] J. Yang, H. Wang, Y. Zhang, H. Zhang, J. Gu, Layered structural PBAT composite foams for efficient electromagnetic interference shielding, Nano-Micro Lett. 16 (2023) 31.
[15] I. Zaporotskova, D. Muratov, L. Kozhitov, A. Popkova, N. Boroznina, S. Boroznin, A. Vasiliev, V. Tarala, E. Korovin, Nanocomposites based on pyrolyzed polyacrylonitrile doped with FeCoCr/C transition metal alloy nanoparticles: synthesis, structure, and electromagnetic properties, Polymers 15 (2023) 3596.
[16] Z. Wang, Q. Fang, J. Li, B. Liu, Y. Liu, Effect of lattice distortion on solid solution strengthening of BCC high-entropy alloys, J. Mater. Sci. Technol. 34 (2018) 349–354.
[17] C.M. Rost, E. Sachet, T. Borman, A. Moballegh, E.C. Dickey, D. Hou, J.L. Jones, S. Curtarolo, J.-P. Maria, Entropy-stabilized oxides, Nat. Commun. 6 (2015) 8485.
[18] J. Dąbrowa, M. Stygar, A. Mikuła, A. Knapik, K. Mroczka, W. Tejchman, M. Danielewski, M. Martin, Synthesis and microstructure of the (Co,Cr,Fe,Mn, Ni)$_3O_4$ high entropy oxide characterized by spinel structure, Mater. Lett. 216 (2018) 32–36.
[19] K. Chen, X. Pei, L. Tang, H. Cheng, Z. Li, C. Li, X. Zhang, L. An, A five-component entropy-stabilized fluorite oxide, J. Eur. Ceram. Soc. 38 (2018) 4161–4164.
[20] Z. Yan, D. Li, X. Zhang, Q. Men, B. Fan, L. Guan, X. Guo, R. Zhang, B. Zhao, Dual-phase high-entropy $(FeCoNiZn)_xV_2O_y$ oxides with promising microwave absorption properties, Ceram. Int. 48 (2022) 36871–36879.
[21] B. Zhao, Z. Yan, Y. Du, L. Rao, G. Chen, Y. Wu, L. Yang, J. Zhang, L. Wu, D. W. Zhang, R. Che, High-entropy enhanced microwave attenuation in titanate perovskites, Adv. Mater. 35 (2023) 2210243.
[22] X. Chang, Z. Duan, D. Wang, S. Wang, Z. Lin, B. Ma, K. Wu, High-entropy spinel ferrites with broadband wave absorption synthesized by simple solid-phase reaction, Molecules 28 (2023) 3468.
[23] B. Quan, W. Gu, J. Sheng, X. Lv, Y. Mao, L. Liu, X. Huang, Z. Tian, G. Ji, From intrinsic dielectric loss to geometry patterns: dual-principles strategy for ultrabroad band microwave absorption, Nano Res. 14 (2020) 1495–1501.
[24] J. Zheng, Z. Sun, W. He, S. Jiang, G. Lou, X. Li, Y. Chen, Enoki-like carbon nanotubes coated with in situ growing nickel particles for enhanced electromagnetic wave absorption, J. Alloys Compd. 960 (2023) 170742.
[25] Z. Sun, J. Shen, Y. Chen, S. Jiang, L. Zhou, X. Li, J. Zheng, Multi-scale heterostructures of MXene-based composites for adjustable electromagnetic wave absorption, J. Alloys Compd. 976 (2024) 173253.
[26] T. Hang, J. Zheng, Y. Zheng, S. Jiang, L. Zhou, Z. Sun, X. Li, G. Tong, Y. Chen, Wheat-like Ni-coated core–shell silver nanowires for effective electromagnetic wave absorption, J. Colloid Interface Sci. 649 (2023) 394–402.
[27] F. Zhang, J. Ju, D. Huo, L. Wu, Y. Lei, Y. Zhang, Photoelectric and photocatalytic properties of long-time annealing Mn-Co-Ni-O thin film, J. Mater. Sci.: Mater. Electron. 34 (2023) 523.
[28] O. Dowinton, M.S. Bahramy, Orbital angular momentum driven anomalous Hall effect, Phys. Rev. B 105 (2022) 235142.
[29] T. Nan, T.J. Anderson, J. Gibbons, K. Hwang, N. Campbell, H. Zhou, Y.Q. Dong, G. Y. Kim, D.F. Shao, T.R. Paudel, N. Reynolds, X.J. Wang, N.X. Sun, E.Y. Tsymbal, S. Y. Choi, M.S. Rzchowski, Y.B. Kim, D.C. Ralph, C.B. Eom, Anisotropic spin-orbit torque generation in epitaxial $SrIrO_3$ by symmetry design, Proc. Natl. Acad. Sci. 116 (2019) 16186–16191.
[30] M.R. Savina, R. Trappitsch, B.H. Isselhardt, Electronic excitation of uranium atoms sputtered from uranium metal and oxides, Spectrochim. Acta Part B: At. Spectrosc. 149 (2018) 214–221.
[31] A. Mubeen, A. Majid, M. Alkhedher, S. Haider, M.S. Akhtar, First principles investigations on electronic and magnetic properties of Fe: SnO monolayer, Opt. Quantum Electron. 55 (2023) 914.
[32] C. Ge, L. Wang, G. Liu, K. Xu, L. Wang, L. Zhang, X. He, Electromagnetic and microwave absorption properties of iron pentacarbonyl pyrolysis-synthesized carbonyl iron fibers, RSC Adv. 10 (2020) 23702–23711.
[33] M.S. Cao, X.X. Wang, M. Zhang, W.Q. Cao, X.Y. Fang, J. Yuan, Variable-temperature electron transport and dipole polarization turning flexible multifunctional microsensor beyond electrical and optical energy, Adv. Mater. 32 (2020) 1907156.
[34] G. Fan, X. Zhang, Q. Wang, R. Su, Y. Tang, C. Hao, Y. Liu, Dielectric evolution of permittivity transition from positive to negative induced by percolation in ceramic composites, Ceram. Int. 49 (2023) 35518–35523.
[35] X. Gao, Z. Dou, R. Peng, X. Wang, Y. Lv, Design of a wideband and tunable radar absorber, Mater. Res. Express 10 (2023) 106301.
[36] M. Cao, J. Yuan, H. Liu, X. Fang, J. Zhu, A simulation of the quasi-standing wave and generalized half-wave loss of electromagnetic wave in non-ideal media, : Mater. Des. 24 (2003) 31–35.
[37] M. Green, X. Chen, Recent progress of nanomaterials for microwave absorption, J. Mater. 5 (2019) 503–541.
[38] Y. Yin, X. Liu, X. Wei, R. Yu, J. Shui, Porous CNTs/Co Composite Derived from zeolitic imidazolate framework: a lightweight, ultrathin, and highly efficient electromagnetic wave absorber, ACS Appl. Mater. Interfaces 8 (2016) 34686–34698.
[39] H. Li, X. Song, H. Gong, L. Tong, X. Zhou, Z. Wang, T. Fan, Prediction of optical properties in particulate media using double optimization of dependent scattering and particle distribution, Nano Lett. 24 (2024) 287–294.
[40] K. Sun, C. Wang, J. Tian, Z. Zhang, N. Zeng, R. Yin, W. Duan, Q. Hou, Y. Zhao, H. Wu, R. Fan, Magnetic-driven broadband epsilon-near-zero materials at radio frequency, Adv. Funct. Mater. 34 (2024) 2306747.
[41] W. Huang, Z. Tong, Y. Bi, M. Ma, Z. Liao, G. Wu, Y. Ma, S. Guo, X. Jiang, X. Liu, Synthesis and microwave absorption properties of coralloid core-shell structure NiS/Ni_3S_4@PPy@MoS_2 nanowires, J. Colloid Interface Sci. 599 (2021) 262–270.
[42] L. Wang, H. Xiong, S. Ur Rehman, Y. Chen, Q. Tan, L. Zhang, M. Zhong, Z. Zhong, Optimized microstructure and impedance matching for improving the absorbing properties of core-shell C@Fe_3C/Fe nanocomposites, J. Alloys Compd. 780 (2019) 552–557.

[43] M. Liu, B. Li, L. Zeng, Y. Wei, R. Wen, X. Zhang, C. Deng, Dynamic tunable narrow-band perfect absorber for fiber-optic communication band based on liquid crystal, J. Phys. D: Appl. Phys. 56 (2023) 505102.
[44] M. Sun, R. Mollaabbasi, B. Li, H. Alamdari, M. Fafard, S.M. Taghavi, Effects of contact angle on single and multiscale bubble motions in the aluminum reduction cell, Ind. Eng. Chem. Res. 58 (2019) 17568–17582.
[45] W. Xing, P. Li, H. Wang, Q. Lei, Y. Huang, J. Fan, G. Xu, The similar Cole-Cole semicircles and microwave absorption of hexagonal Co/C composites, J. Alloys Compd. 750 (2018) 917–926.
[46] X. Fu, Q. Zheng, L. Li, M. Cao, Vertically implanting $MoSe_2$ nanosheets on the RGO sheets towards excellent multi-band microwave absorption, Carbon 197 (2022) 324–333.
[47] K. Sun, X. Yang, Y. Lei, H. Du, T. Dudziak, R. Fan, Core-shell structural design and microwave absorption enhancement of multi-dimensional graphene oxide@polypyrrole/carbonyl iron fiber nanocomposites, J. Alloys Compd. 930 (2023) 167446.
[48] K. Sun, Z. Zhang, J. Tian, N. Zeng, B. Wang, W. Xing, L. Ma, Y. Long, C. Wang, R. Fan, Flexible and biocompatible polyurethane/Co@C composite films with weakly negative permittivity, advanced composites and hybrid, Materials 7 (2024) 22.
[49] Y. Yang, C. Xu, Y. Xia, T. Wang, F. Li, Synthesis and microwave absorption properties of FeCo nanoplates, J. Alloys Compd. 493 (2010) 549–552.